

An Integrated Inductor for Parallel Interleaved VSCs and PWM Schemes for Flux Minimization

Gohil, Ghanshyamsinh Vijaysinh; Bede, Lorand; Teodorescu, Remus; Kerekes, Tamas; Blaabjerg, Frede

Published in:
I E E E Transactions on Industrial Electronics

DOI (link to publication from Publisher):
[10.1109/TIE.2015.2455059](https://doi.org/10.1109/TIE.2015.2455059)

Creative Commons License
Unspecified

Publication date:
2015

Document Version
Early version, also known as pre-print

[Link to publication from Aalborg University](#)

Citation for published version (APA):
Gohil, G. V., Bede, L., Teodorescu, R., Kerekes, T., & Blaabjerg, F. (2015). An Integrated Inductor for Parallel Interleaved VSCs and PWM Schemes for Flux Minimization. *I E E E Transactions on Industrial Electronics*, 62(12), 7534 - 7546. <https://doi.org/10.1109/TIE.2015.2455059>

General rights

Copyright and moral rights for the publications made accessible in the public portal are retained by the authors and/or other copyright owners and it is a condition of accessing publications that users recognise and abide by the legal requirements associated with these rights.

- Users may download and print one copy of any publication from the public portal for the purpose of private study or research.
- You may not further distribute the material or use it for any profit-making activity or commercial gain
- You may freely distribute the URL identifying the publication in the public portal -

Take down policy

If you believe that this document breaches copyright please contact us at vbn@aub.aau.dk providing details, and we will remove access to the work immediately and investigate your claim.

An Integrated Inductor for Parallel Interleaved VSCs and PWM Schemes for Flux Minimization

Ghanshyamsinh Gohil, *Student Member, IEEE*, Lorand Bede, *Student Member, IEEE*,
Remus Teodorescu, *Fellow, IEEE*, Tamas Kerekes, *Member, IEEE*, and Frede Blaabjerg, *Fellow, IEEE*,

Abstract—The interleaving of the carrier signals of the parallel Voltage Source Converters (VSCs) can reduce the harmonic content in the resultant switched output voltages. As a result, the size of the line filter inductor can be reduced. However, in addition to the line filter, an inductive filter is often required to suppress the circulating current. The size of the system can be reduced by integrating these two inductors in a single magnetic component. A integrated inductor, which combines the functionality of both the line filter inductor and the circulating current filter inductor is presented. The PulseWidth Modulation (PWM) schemes to reduce the flux in some parts of the integrated inductor are also analyzed. The flux reduction achieved by using these schemes is demonstrated by comparing these schemes with the conventional space vector modulation and the 60° clamped discontinuous PWM scheme. The impact of these PWM schemes on the harmonic performance is also discussed. Simulation and experimental results are presented to validate the analysis.

Index Terms—Voltage Source Converters (VSC), parallel, interleaving, filter design, pulse-width modulation, integrated inductor

I. INTRODUCTION

Voltage Source Converters (VSCs) are often connected in parallel in many high power applications. The harmonic quality of the resultant voltage waveforms in such systems can be improved by interleaving the carrier signals of the parallel connected VSCs [1]–[3]. This leads to size reduction of the line filter inductor through the improvement in the output voltage quality. However, when VSCs are connected in parallel, the circulating current flows through the closed path due to the control asymmetry and the impedance mismatch. When the carriers are interleaved, the pole voltages (switched output voltage of the VSC leg, measured with respect to the dc-link mid-point O) of the interleaved parallel legs are phase shifted. This instantaneous potential difference further increases the circulating current, which would result in increased losses and unnecessary over-sizing of the components present in the circulating current path. Therefore, the circulating current should be suppressed to realize the full potential of the interleaved carriers in parallel connected VSCs.

The formation of the circulating current path can be avoided

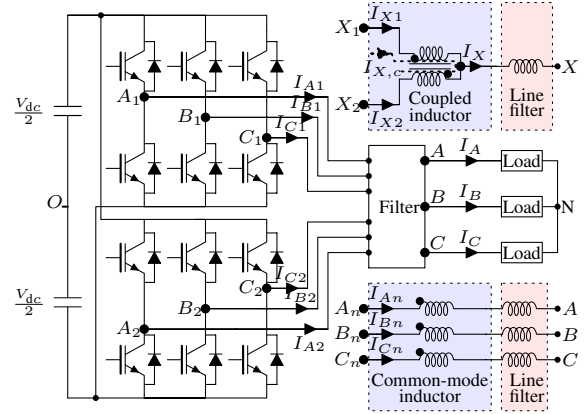


Fig. 1. Two parallel interleaved VSCs with a common dc-link. The filter arrangement for circulating current suppression using the CI and the CM inductor is depicted, where $X = \{A, B, C\}$ and $n = \{1, 2\}$.

by using the line frequency isolation transformer [4]. However, it increases the overall size of the system and should be avoided. The use of the Common-Mode (CM) inductor in series with the line filter inductor for each of the VSCs is proposed in [2], as shown in Fig. 1. Another approach proposes the use of the Coupled Inductor (CI) to suppress the circulating current by providing magnetic coupling between the parallel interleaved legs of the corresponding phases [1], [5] is also shown in Fig. 1. A Pulse Width Modulation (PWM) scheme to reduce the peak value of the flux density in the CI is presented in [6], where the common mode signal, which is added to the reference voltage waveforms, has been optimized. Ewanchuk *et al.* [7] proposed the integration of three different CIs into one three-limb core. However, in order to suppress the circulating current using the three-limb core, the CM voltage difference between the two parallel VSCs should be made zero. This was achieved by employing a modified Discontinuous PulseWidth Modulation (DPWM) scheme, which has more number of commutations than the conventional (both the continuous and the discontinuous) modulation schemes. Therefore, this scheme may not be feasible for medium/high power applications.

In all of the above discussed approaches, two distinct magnetic components are involved:

- 1) Line filter inductor (commonly referred as a boost inductor) for improving the line current quality.
- 2) Additional inductive components (CI / CM inductor) for suppressing the circulating current.

Manuscript received January 26, 2015; revised April 13, 2015 and May 14, 2015; accepted June 13, 2015.

Copyright © 2015 IEEE. Personal use of this material is permitted. However, permission to use this material for any other purposes must be obtained from the IEEE by sending a request to pubs-permissions@ieee.org. This work was supported by the Innovation Foundation Denmark through the Intelligent Efficient Power Electronics (IEPE) technology platform.

The authors are with the Department of Energy Technology, Aalborg University, 9220 Aalborg East, Denmark (e-mail: gvg@et.aau.dk).

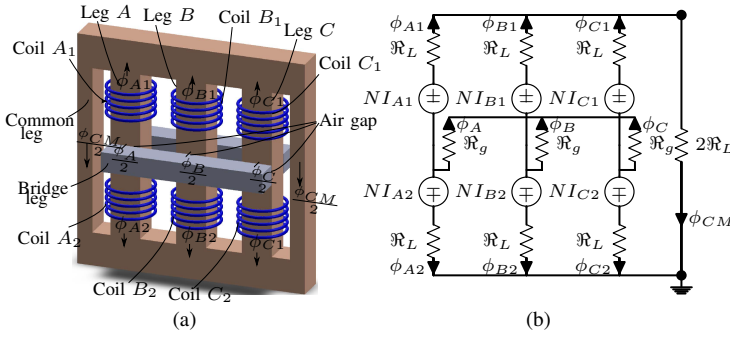


Fig. 2. Magnetic structure of the proposed integrated three-phase inductor. (a) Physical arrangement, (b) Simplified reluctance model of the proposed integrated three-phase inductor.

The improvement in the power density can be achieved by integrating both of these inductors in a single magnetic structure.

This paper presents an integrated three-phase inductor for the parallel interleaved VSCs, which integrates three CIs and a three phase line filter inductor in a single magnetic structure. The analysis of the integrated three-phase inductor is given in Section II. Optimized PWM schemes to reduce the flux in some parts of the proposed inductor are discussed in Section III and their impact on the line current quality is evaluated in Section IV. A design example of an integrated inductor is presented in Section V. Finally, Section VI summarizes simulations and experimental results.

II. INTEGRATED INDUCTOR

The magnetic structure of the proposed integrated inductor, which combines the functionality of three separate CIs and the three-phase line filter inductor, is shown in Fig. 2(a). The core is composed of three inner legs (referred as a phase leg), two outer common legs and two bridge legs which facilitate the magnetic coupling between the phases. The coils of a particular phase of both of the parallel VSCs are wound on the same phase leg with opposite winding directions. A high permeability material is used for the phase legs and the common legs, whereas the bridge legs are realized using laminated iron core. Necessary air gaps have been inserted between the bridge leg and the phase legs.

A. Simplified Reluctance Model

A simplified reluctance model of the integrated inductor is shown in Fig. 2(b). The reluctance of half of the phase leg is taken to be \mathcal{R}_L and the reluctance of each of the air gap is termed as $2\mathcal{R}_g$. The equivalent reluctance of each bridge leg is the addition of the reluctance of the air gap ($\mathcal{R}_g = 2\mathcal{R}_g \parallel 2\mathcal{R}_g$) and the reluctance of the laminated iron core of that bridge. However, the reluctance of the laminated steel core is very small compared to the equivalent reluctance of the air gap \mathcal{R}_g . Therefore, the reluctance of each bridge leg is approximated as \mathcal{R}_g , as shown in Fig. 2(b). In addition, the magnetic asymmetry introduced by the yokes of the high permeability magnetic material is also neglected.

The coils are represented by the equivalent Magneto-Motive

Forces (MMFs) in the simplified reluctance model. The MMF of each coil is proportional to the current flowing through that coil. Therefore, the involved current quantities are first defined and then the reluctance network is solved in order to obtain the flux linkage associated with each of the coils.

In parallel interleaved VSCs, the current flowing through the coil has a circulating current component ($I_{x,c}$) and a line current component $I_{x,l}$. Assuming ideal VSCs and neglecting the effect of the hardware/control asymmetries, the line current component of each of the VSCs are considered to be equal and it is given as

$$I_{x,l} = \frac{I_x}{2} \quad (1)$$

where $x = \{A, B, C\}$ and I_x is the resultant line current. Therefore, the coil currents can be expressed as

$$I_{x1} = \frac{I_x}{2} + I_{x,c} \text{ and } I_{x2} = \frac{I_x}{2} - I_{x,c} \quad (2)$$

where $I_{x,c}$ is the circulating current. Using (2), the circulating current is obtained as

$$I_{x,c} = \frac{I_{x1} - I_{x2}}{2} \quad (3)$$

The CM current is defined as

$$I_{CM,n} = \frac{I_{An} + I_{Bn} + I_{Cn}}{3} \quad (4)$$

where $n=\{1,2\}$. Using (3) and (4), the CM circulating current $I_{CM,c}$ is given by

$$I_{CM,c} = \frac{I_{CM,1} - I_{CM,2}}{2} = \frac{I_{A,c} + I_{B,c} + I_{C,c}}{3} \quad (5)$$

By solving the simplified reluctance network, the flux in the phase legs are

$$\begin{aligned} \phi_{x1} &\approx \frac{1}{2(\mathcal{R}_L + 2\mathcal{R}_g)} NI_x + \frac{1}{\mathcal{R}} NI_{x,c} - \frac{3}{4\mathcal{R}} NI_{CM,c} \\ \phi_{x2} &\approx \frac{1}{2(\mathcal{R}_L + 2\mathcal{R}_g)} NI_x - \frac{1}{\mathcal{R}} NI_{x,c} + \frac{3}{4\mathcal{R}} NI_{CM,c} \end{aligned} \quad (6)$$

The CM flux component is given as

$$\phi_{CM} \approx \frac{3}{4\mathcal{R}_L} NI_{CM,c} \quad (7)$$

and the flux in the common leg is half of the CM flux $\phi_{CM}/2$. The flux in the air gaps is given as

$$\phi_x \approx -\frac{1}{\mathcal{R}_L + 2\mathcal{R}_g} NI_x \quad (8)$$

B. Line Filter Inductance L_f

Using (6), the voltage across the coil $x1$ can be obtained as

$$\int V_{x1x} dt = \frac{N^2}{2(\mathcal{R}_L + 2\mathcal{R}_g)} I_x + \frac{N^2}{\mathcal{R}} I_{x,c} - \frac{3N^2}{4\mathcal{R}} I_{CM,c} \quad (9)$$

Similarly, the voltage across across the coil $x2$ is given as

$$\int V_{x2x} dt = \frac{N^2}{2(\mathcal{R}_L + 2\mathcal{R}_g)} I_x - \frac{N^2}{\mathcal{R}} I_{x,c} + \frac{3N^2}{4\mathcal{R}} I_{CM,c} \quad (10)$$

Averaging the voltages across the coils of the respective phases

$$V_{avg} = L_f \frac{d}{dt} I + V_g \quad (11)$$

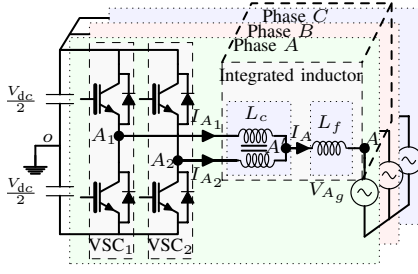


Fig. 3. Parallel interleaved VSCs with the proposed integrated inductor.

where

$$\mathbf{V}_{avg} = \left[\frac{V_{A1O} + V_{A2O}}{2} \quad \frac{V_{B1O} + V_{B2O}}{2} \quad \frac{V_{C1O} + V_{C2O}}{2} \right]^T \quad (12)$$

$$\mathbf{V}_g = [V_{Ag} \quad V_{Bg} \quad V_{Cg}]^T, \quad \mathbf{I} = [I_A \quad I_B \quad I_C]^T \quad (13)$$

$$\mathbf{L}_f = \frac{N^2}{6(\mathcal{R}_L + 2\mathcal{R}_g)} \begin{bmatrix} 2 & -1 & -1 \\ -1 & 2 & -1 \\ -1 & -1 & 2 \end{bmatrix} \quad (14)$$

Differential equation (11) describes the dynamics of the resultant line current. For a three-phase balance system

$$I_A + I_B + I_C = 0 \quad (15)$$

Using (11) and (15), the average value of the flux linkage of the respective phase is given as

$$\int \left(\frac{V_{x1O} + V_{x2O}}{2} \right) dt = \frac{N^2}{2(\mathcal{R}_L + 2\mathcal{R}_g)} I_x + V_{xg} \quad (16)$$

and the inductance offered to the line current is given as

$$L_f \approx \frac{N^2}{2(\mathcal{R}_L + 2\mathcal{R}_g)} \approx \frac{N^2}{4\mathcal{R}_g} \quad (17)$$

Let, the length of each of the air gap be l_g and the effective cross-sectional area of the gap is A_g . Then (17) can be rewritten as

$$L_f \approx \frac{\mu_0 N^2 A_g}{2l_g} \quad (18)$$

C. Circulating Current Filter Inductance L_c

The circulating current is proportional to the time integral of the difference of the pole voltages of the parallel legs. For the proposed integrated inductor, the differential equations that describe the behavior of the circulating current is obtained from (9) and (10) and it is given as

$$\Delta \mathbf{V} = \mathbf{L}_c \frac{d}{dt} \mathbf{I}_c \quad (19)$$

$$\text{where } \Delta \mathbf{V} = [\Delta V_A \quad \Delta V_B \quad \Delta V_C]^T \quad (20)$$

$$\mathbf{I}_c = [I_{A,c} \quad I_{B,c} \quad I_{C,c}]^T \quad (21)$$

$$\mathbf{L}_c = \frac{N^2}{2\mathcal{R}_L} \begin{bmatrix} 3 & -1 & -1 \\ -1 & 3 & -1 \\ -1 & -1 & 3 \end{bmatrix} \quad (22)$$

where $\Delta V_x = V_{x1O} - V_{x2O}$ and $x = \{A, B, C\}$. As given in (19), the value of the \mathbf{L}_c is independent of the air gap geometry and depends only on the values of the reluctance of

the phase legs and the common legs. The circulating current can effectively be suppressed by reducing the reluctance of the phase legs and the common legs.

Using (11) and (19), electrical equivalent circuit of the parallel interleaved VSCs with the proposed integrated inductor is derived, as shown in Fig. 3.

D. Flux Linkage in the Common Legs

The common legs in the proposed integrated inductor are required to provide the return path for the common flux components of the circulating flux of all three phases. The size of the proposed integrated inductor can be further reduced by reducing the peak value of the flux in the common legs. The flux in the common leg depends on the reluctance of the common leg, the number of turns, and the CM circulating current $I_{CM,c}$, as shown in (7). The CM circulating current $I_{CM,c}$ is proportional to the time integral of the CM voltage difference of the parallel VSCs.

In order to present a general analysis (independent of the number of turns N), the CM flux linkage is analyzed. Using (6) and (7), the CM flux linkage is derived, and it is given as

$$\lambda_{CM}(t) = \frac{3}{2} \int \Delta V_{CM} dt \quad (23)$$

where ΔV_{CM} is the CM voltage difference of both the VSCs ($V_{CM,1} - V_{CM,2}$). Therefore, the flux density in the common leg can be reduced by decreasing the $\int \Delta V_{CM} dt$.

III. PWM SCHEMES

The size reduction of the proposed integrated inductor can be achieved by reducing the peak value of the λ_{CM} . PWM schemes to reduce the peak value of the λ_{CM} are discussed in this Section. The improvement achieved by using these schemes is demonstrated by comparing the peak value of the λ_{CM} of these schemes with that of the center aligned Space Vector Modulation (SVM) and the 60° clamped discontinuous modulation (DPWM1) [8]. The analysis is carried for the interleaving angle of 180°, as it results in optimal harmonic performance at high modulation indices.

A. Conventional PWM Schemes

In a conventional SVM, VSC cycles through four switch states in each switching cycle. Based on the position of the reference space vector (\vec{V}_{ref}), two adjacent active voltage vectors and both of the zero voltage vectors (\vec{V}_0, \vec{V}_7) are applied to synthesize \vec{V}_{ref} . Out of the two zero voltage vectors, one is redundant and can be omitted. As a result, several DPWM schemes have emerged. In both the SVM and the DPWM, at least one zero voltage vector is used in each switching cycle. The use of the zero vector would lead to the maximum value of the CM voltage of $\pm V_{dc}/2$. For the parallel interleaved VSCs with an interleaving angle of 180°, the use of the SVM would result in maximum value of the ΔV_{CM} to be $\pm V_{dc}$, whereas for DPWM schemes, this value is $\pm 2V_{dc}/3$ [9]. From (23), it is evident that the flux in the common leg can be reduced by reducing the time integral of the ΔV_{CM} . This can be achieved by avoiding the use of zero voltage vectors.

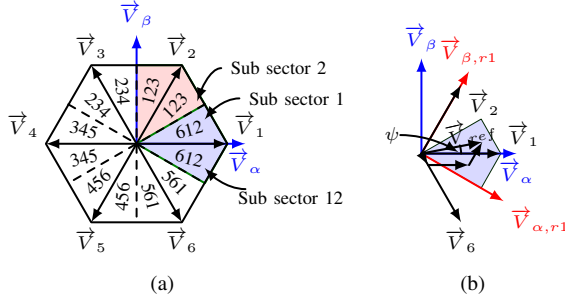


Fig. 4. NSPWM. (a) Switching sequences involved in the near state PWM. Numbers represents the switching sequence, (b) Formation of a reference space vector \vec{V}_{ref} by the geometrical summation of the three nearest voltage vectors in the region 1.

B. Reduced CM Voltage PWM Schemes

Several PWM schemes, which do not use zero vectors to synthesize the \vec{V}_{ref} , are reported in the literature [10]. Out of these reported schemes, the most suitable schemes for parallel interleaved VSCs with the proposed integrated inductor are identified and their effect on the λ_{CM} is discussed.

An Active Zero State PWM (AZSPWM) scheme uses two adjacent active voltage vectors and two near opposing active vectors [11]–[14]. The active voltage vectors that are 120° apart are used in a Remote State PWM (RSPWM) scheme [15]. However, the number of commutations in a switching cycle is increased compared to that of the SVM and may not be feasible in high power applications due to the high switching losses. A Near State PWM (NSPWM) employs three nearest active voltage vectors to synthesize the \vec{V}_{ref} [16], [17]. Out of these PWM schemes, the AZSPWM and the NSPWM are adopted to modulate the parallel interleaved VSCs because of their superior harmonic performance, as discussed in Section IV.

1) *Near State PWM*: The NSPWM scheme employs three nearest active voltage vectors to synthesize the reference voltage vector \vec{V}_{ref} . Fig. 4(a), shows the switching sequences used in the different sectors of the space vector diagram, where the number represents the sequence in which the corresponding voltage vectors are applied. Depending on the switching sequences involved, the space vector diagram is divided into six regions. The switching sequence 612 is used in both sub-sector 1 ($0^\circ \leq \psi < 30^\circ$) and sub-sector 12 ($330^\circ \leq \psi < 360^\circ$) and these two sub-sector together constitute region 1.

The geometrical formation of the \vec{V}_{ref} in region 1 is depicted in Fig. 4(b). The active voltage vectors \vec{V}_1, \vec{V}_2 , and \vec{V}_6 are used and their respective dwell times are given as

$$T_1 = (\sqrt{3} \frac{V_{\alpha,r}}{V_{dc}} + \frac{V_{\beta,r}}{V_{dc}} - 1)T_s \quad (24a)$$

$$T_2 = (1 - \frac{2}{\sqrt{3}} \frac{V_{\alpha,r}}{V_{dc}})T_s \quad (24b)$$

$$T_6 = (1 - \frac{1}{\sqrt{3}} \frac{V_{\alpha,r}}{V_{dc}} - \frac{V_{\beta,r}}{V_{dc}})T_s \quad (24c)$$

where $V_{\alpha,r}$ and $V_{\beta,r}$ are the α and β components at the start of the region. For the region 1, these components are given as

$$V_{\alpha,r1} = \frac{\sqrt{3}}{2}V_\alpha - \frac{1}{2}V_\beta, \quad V_{\beta,r1} = \frac{1}{2}V_\alpha + \frac{\sqrt{3}}{2}V_\beta \quad (25)$$

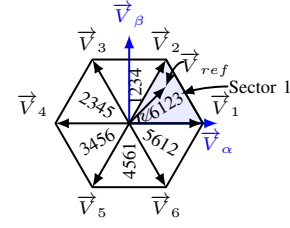


Fig. 5. Switching sequences involved in the active zero state PWM.

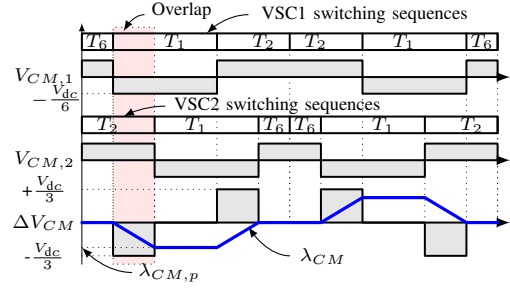


Fig. 6. Switching sequences and CM voltages of both the VSCs with an interleaving angle of 180° in sub-sector 1 ($30^\circ \leq \psi < 60^\circ$) for the NSPWM.

Let the modulation index M be the ratio of the amplitude of the reference phase voltage to the half of the dc-link voltage. In NSPWM, the value of M should not fall below 0.769 in order to ensure positive dwell times of the active voltage vectors. Therefore, the modulation index M should be restricted within a range of 0.769 to 1.154, which is sufficient for most grid-connected applications in a normal operating mode. However, the VSC is required to operate in a low modulation index region during the low voltage ride through and AZSPWM is used in this region.

2) *AZSPWM Scheme*: The adjacent active voltage vectors and the two near opposing active voltage vectors are used to formulate the reference voltage vector \vec{V}_{ref} [11]–[13]. The switching sequences involved in the AZSPWM are shown in Fig. 5. The discussion is only restricted to sector 1 ($0^\circ \leq \psi < 60^\circ$) due to the symmetry. The active voltage vectors $\vec{V}_1, \vec{V}_2, \vec{V}_3$, and \vec{V}_6 are used in sector 1, and their respective dwell times are given as

$$T_1 = \frac{2}{\sqrt{3}} \frac{|\vec{V}_{ref}|}{V_{dc}} T_s \sin(60^\circ - \psi) \quad (26a)$$

$$T_2 = \frac{2}{\sqrt{3}} \frac{|\vec{V}_{ref}|}{V_{dc}} T_s \sin(\psi) \quad (26b)$$

$$T_3 = T_6 = (T_s - T_1 - T_2)/2 \quad (26c)$$

The dwell time of the adjacent active vectors (T_1, T_2) is the same as that of the conventional SVM. However, instead of using the zero vectors, two near opposing active voltage vectors (\vec{V}_3, \vec{V}_6) are used. As a result, the linear operation over the entire modulation range ($0 \leq M < 2/\sqrt{3}$) is achieved.

C. Flux Linkage

1) *NSPWM*: The CM voltage of the individual VSC ($V_{CM,1}$ and $V_{CM,2}$) and their difference ΔV_{CM} are shown in Fig. 6. Due to the use of only active vectors, the maximum

TABLE I
MAXIMUM VALUE OF THE PEAK CM FLUX LINKAGE

PWM	Max of the peak CM flux linkage ($\lambda_{CM,pmax}$)
NSPWM	$\lambda_{CM,pmax} = \frac{V_{dc}T_s}{16} \left(3M \sin \left[\arccos \left(\frac{1}{\sqrt{3}M} \right) \right] - 1 \right)$ for $(0.769 \leq M \leq \frac{2}{\sqrt{3}})$
AZSPWM	$\lambda_{CM,pmax} = \frac{V_{dc}T_s}{12} \left(1 - \frac{3}{4}M \right)$ for $(0 \leq M \leq \frac{8}{3+4\sqrt{3}})$ $\lambda_{CM,pmax} = \frac{V_{dc}T_s}{12} \left(\sqrt{3}M - 1 \right)$ for $(\frac{8}{3+4\sqrt{3}} \leq M \leq \frac{2}{\sqrt{3}})$

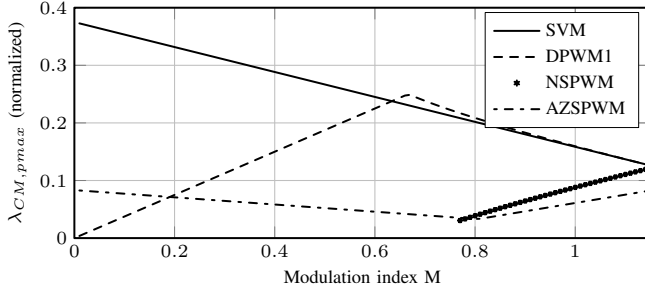


Fig. 7. The variation of the maximum value of the flux linkage in the common leg as a function of the modulation index. The $\lambda_{CM,pmax}$ is normalized with respect to the $V_{dc}T_s$. For the NSPWM, the $\lambda_{CM,pmax}$ is plotted only for the linear modulation range of $0.769 \leq M \leq 1.154$.

CM voltage of the individual VSCs is limited to $\pm V_{dc}/6$. The application of voltage vectors \vec{V}_1 and \vec{V}_2 results in the equal and opposite polarity CM voltages. Due to the opposite polarity of the individual CM voltages, the simultaneous application of \vec{V}_1 in VSC1 and \vec{V}_2 in VSC2 and vice-versa in sub sector 1 forces the difference in CM voltages ΔV_{CM} to take the value of $\pm V_{dc}/3$. Therefore, for a given dc-link voltage, the peak value of the flux linkage in a switching cycle ($\lambda_{CM,p}$) depends on the overlap time of the voltage vectors \vec{V}_1 and \vec{V}_2 , as shown in Fig. 6. Similarly, when the \vec{V}_{ref} is in sub sector 12, the overlap time of the voltage vectors \vec{V}_1 and \vec{V}_6 decides the value of the $\lambda_{CM,p}$.

The value of the $\lambda_{CM,p}$ changes with every update of the reference voltage vector \vec{V}_{ref} (varies with the space vector angle ψ , and therefore has different values in each switching cycle). The maximum value out of the $\lambda_{CM,p}$ values over a 60° region of the space diagram is denoted as $\lambda_{CM,pmax}$ and it is given in Table I.

2) **AZSPWM**: The variation of the $\lambda_{CM,pmax}$ over a 60° region of the space diagram for the AZSPWM is also given in Table I.

The variation in the $\lambda_{CM,pmax}$ with respect to the modulation index M for both the NSPWM and the AZSPWM is plotted in Fig. 7 and compared with that of the SVM and the 60° clamped DPWM (commonly referred as a DPWM1) schemes. The equations for $\lambda_{CM,pmax}$ as a function of modulation index M for the SVM and the DPWM1 are derived in [9] and the variation of the $\lambda_{CM,pmax}$ is plotted in Fig. 7 for the sake of comparison. The maximum values of the

TABLE II
MAXIMUM VALUE OF THE CM FLUX LINKAGE OVER THE ENTIRE LINEAR MODULATION RANGE

PWM	Maximum flux-linkage (normalized)	Reduction
SVM	0.37 ($M = 0$)	100%
DPWM1	0.25 ($M = 2/3$)	67%
NSPWM	0.12 ($M = \frac{2}{\sqrt{3}}$)	32%
AZSPWM	0.082 ($M = 0, M = \frac{2}{\sqrt{3}}$)	22%

TABLE III
THE POLARITY OF THE CARRIER SIGNALS OF EACH OF THE PHASES OF THE INDIVIDUAL VSCs IN SECTOR 1 ($0^\circ \leq \psi < 60^\circ$) FOR THE SVM AND THE AZSPWM AND IN REGION 1 FOR THE DPWM1 AND THE NSPWM

Carrier Phase	SVM / DPWM1 VSC1	SVM / DPWM1 VSC2	AZSPWM VSC1	AZSPWM VSC2	NSPWM VSC1	NSPWM VSC2
A	+ve	-ve	-ve	+ve	+ve	-ve
B	+ve	-ve	+ve	-ve	+ve	-ve
C	+ve	-ve	-ve	+ve	-ve	+ve

CM flux linkage for the entire linear modulation range for each of the PWM schemes are shown in Table II. The CM flux linkage values are normalized with respect to the $V_{dc}T_s$. Considering the maximum value of the CM flux linkage of the SVM as a base value, the reduction achieved by other PWM schemes is given in Table II. A considerable reduction in the maximum CM flux-linkage is achieved using the AZSPWM (78% reduction compared to SVM and 66% reduction compared to the DPWM1). The use of the NSPWM also results in substantial reduction in the maximum value of the CM flux-linkage.

IV. ASSESSMENT OF THE LINE CURRENT QUALITY

The impact of the switching sequences of the NSPWM and the AZSPWM on the line current quality is analyzed in this section.

A. Pulse Patterns

The use of NSPWM and AZSPWM is limited in a single VSC system as the line-to-line voltage pulses exhibits bipolar pattern and results in more ripple in the line current [17]. However, in the case of the parallel interleaved VSCs, the pulse pattern of the resultant line-to-line voltage can be significantly improved by using an interleaving angle of 180° , as explained in this subsection.

The scalar implementation of the AZSPWM requires two opposite polarity carrier signals. The modulation waveforms are the same as that of the SVM and the carrier waveforms are selected based on the reference space vector angles [18]. For the parallel interleaved VSCs, the selection of the carrier signals to modulate each of the phases in sector 1 ($0^\circ \leq \psi < 60^\circ$) for the SVM and the AZSPWM scheme are shown in Table III. The use of the same modulation signal and the same carrier signals for phase B in both the PWM schemes yields the same pole voltages of phase B. However, the carrier signals of phase A and phase C in AZSPWM have opposite polarity than the SVM. As a result, the pole voltages of phase A and phase C of the individual VSCs are different in the SVM and the

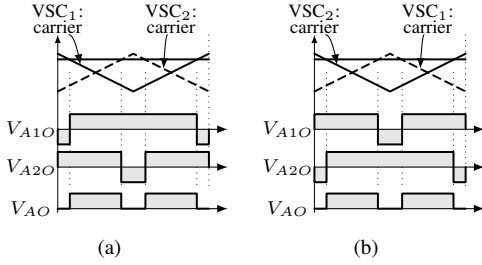


Fig. 8. Pole voltages of phase A of individual VSCs and their average with $M = 1$ and $\psi = 20^\circ$. (a) SVM, (b) AZSPWM.

AZSPWM. For the parallel VSCs, the resultant pole voltage is an average of the pole voltages of the individual VSCs. The pole voltages of the individual VSCs and the resultant pole voltage for phase A for the SVM and the AZSPWM are shown in Fig. 8 and it is evident that the resultant pole voltages are the same in both the cases. Therefore, for the parallel interleaved VSCs with an interleaving angle 180° , the resultant pole voltages of all the phases are the same for both the SVM and the AZSPWM. As a result, the harmonic performance of the parallel interleaved VSCs modulated using the AZSPWM is also the same as that of the SVM.

Similarly, the NSPWM scheme can be realized by using the modulation waveforms of the DPWM1 and by using two carrier signals with opposite polarities [18]. For an interleaving angle of 180° , the polarity of the carrier signals of each of the phases of the individual VSCs in region 1 ($330^\circ \leq \psi < 360^\circ$ and $0^\circ \leq \psi < 30^\circ$) for the NSPWM and the DPWM1 schemes are given in Table III. Due to the use of the same modulation waveform and the same carrier signals in region 1, the pole voltages of phase A and phase B are the same for both the PWM schemes. In NSPWM, phase C is modulated using the opposite polarity carrier than that of the DPWM1 and therefore the pole voltages of phase C of the individual VSCs are different in both the schemes. However, the average of the pole voltages of phase C is the same for both of the PWM schemes. As a result, the harmonic performance of the parallel interleaved VSCs, modulated using the NSPWM, is also the same as that of the DPWM1.

B. Harmonic Performance

As a result of the modulation, the pole voltages have undesirable harmonic components in addition to the required fundamental component. These harmonic components can be represented as the summation series of sinusoids, characterized by the carrier index variable m and the baseband index variable n [8]. The h th harmonic component is defined in terms of m and n , and it is given as

$$h = m\left(\frac{\omega_c}{\omega_0}\right) + n \quad (27)$$

where ω_0 is the fundamental frequency and ω_c is the carrier frequency.

The harmonic coefficients A_{mn} and B_{mn} in (28) are evaluated for each 60° sextant using the double Fourier integral. The harmonic coefficients for this case are given in (29) and (30).

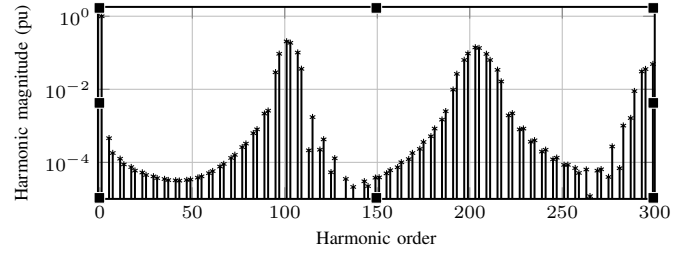


Fig. 9. Theoretical harmonic spectra of the line-to-line output voltage of the parallel interleaved VSCs with interleaving angle of 180° , modulated using AZSPWM with modulation index of $M = 1$ and the carrier ratio $(\omega_c/\omega_0)=51$.

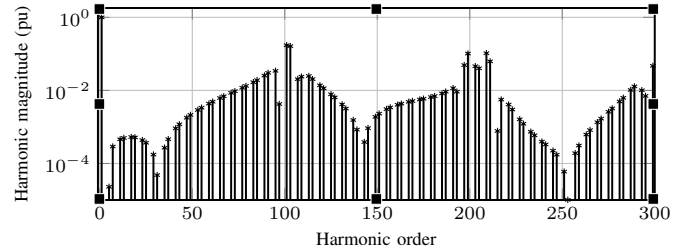


Fig. 10. Theoretical harmonic spectra of the line-to-line output voltage of the parallel interleaved VSCs with interleaving angle of 180° , modulated using NSPWM with modulation index of $M = 1$ and the carrier ratio $(\omega_c/\omega_0)=51$.

The expressions contain $J_y(z)$, which represents the Bessel functions of the first kind of the order y and argument z . The double summation term in (28) is the ensemble of all possible frequencies, formed by taking the sum and the difference between the carrier harmonics, the fundamental waveform and its associated baseband harmonics.

The theoretical closed form harmonic solution of the line-to-line voltage for the AZSPWM is obtained by using (29) and (30) and the harmonic spectrum is shown in Fig. 9. The magnitude of the odd multiple of the carrier harmonics and the associated sideband harmonic components are very small. The major harmonic components appear at the even multiple of the carrier harmonics and its odd sideband harmonics.

The harmonic coefficients of NSPWM are also evaluated in a similar manner and the theoretical harmonic spectrum for $M = 1$ is shown in Fig. 10. In contrast to the AZSPWM, the magnitude of the even multiple of the carrier harmonic components and its sidebands is reduced considerably. However, the roll-off in magnitude of the sideband harmonic components is slower than for the AZSPWM. The harmonic performance of both of the PWM schemes is compared by evaluating the Normalized Weighted Total Harmonic Distortion (NWTHD), which is defined as

$$\text{NWTHD} = \frac{M \sqrt{\sum_{h=2}^{\infty} (V_h/h)^2}}{V_f} \quad (31)$$

where V_f is the fundamental component and V_h is the magnitude of the h th harmonic component.

The NWTHD for all of the PWM schemes are shown in Fig. 11. The resultant pole voltages of the two parallel interleaved VSCs with an interleaving angle of 180° are the same in SVM

$$\begin{aligned}
 f(t) = & \frac{A_{00}}{2} + \sum_{n=1}^{\infty} [A_{0n} \cos(n[\omega_0 t + \theta_0]) + B_{0n} \sin(n[\omega_0 t + \theta_0])] \\
 & + \sum_{m=1}^{\infty} [A_{m0} \cos(m[\omega_c t + \theta_c]) + B_{m0} \sin(m[\omega_c t + \theta_c])] \\
 & + \sum_{m=1}^{\infty} \sum_{\substack{n=-\infty \\ n \neq 0}}^{\infty} [A_{mn} \cos(m[\omega_c t + \theta_c] + n[\omega_0 t + \theta_0]) + B_{mn} \sin(m[\omega_c t + \theta_c] + n[\omega_0 t + \theta_0])]
 \end{aligned} \tag{28}$$

$$A_{mn_{AZS}} = \frac{4V_{dc}}{q\pi^2} \times \left(\begin{aligned} & \frac{\pi}{6} \cos(m\frac{\pi}{2}) \sin(n\frac{\pi}{2}) [1 - \cos(2n\frac{\pi}{3})] \{J_n(q\frac{3\pi}{4}M) + 2\cos(\frac{n\pi}{6})J_n(q\frac{\sqrt{3}\pi}{4}M)\} \\ & + \sum_{\substack{k=1 \\ k \neq -n}}^{\infty} \frac{1}{n+k} \cos(m\frac{\pi}{2}) \sin(k\frac{\pi}{2}) \cos\left([n+k]\frac{\pi}{2}\right) \sin\left([n+k]\frac{\pi}{6}\right) \\ & \times \left\{ J_k(q\frac{3\pi}{4}M) [1 - \cos([n+3k]\frac{\pi}{3})] + 2 \left[\cos\left([2n+3k]\frac{\pi}{6}\right) - \cos\left([n-3k]\frac{\pi}{6}\right) \cos(n\frac{\pi}{6}) \right] \left\{ J_k(q\frac{\sqrt{3}\pi}{4}M) \right\} \right. \\ & \left. + \sum_{\substack{k=1 \\ k \neq n}}^{\infty} \frac{1}{n-k} \cos(m\frac{\pi}{2}) \sin(k\frac{\pi}{2}) \cos\left([n-k]\frac{\pi}{2}\right) \sin\left([n-k]\frac{\pi}{6}\right) \right. \\ & \left. \times \left\{ J_k(q\frac{3\pi}{4}M) [1 - \cos([n-3k]\frac{\pi}{3})] + 2 \left[\cos\left([2n-3k]\frac{\pi}{6}\right) - \cos\left([n+3k]\frac{\pi}{6}\right) \cos(n\frac{\pi}{6}) \right] \left\{ J_k(q\frac{\sqrt{3}\pi}{4}M) \right\} \right\} \right) \end{aligned} \right) \tag{29}$$

$$B_{mn_{AZS}} = \frac{4V_{dc}}{q\pi^2} \times \left(\begin{aligned} & \frac{\pi}{6} \cos(m\frac{\pi}{2}) \sin(n\frac{\pi}{2}) \sin(2n\frac{\pi}{3}) \{J_n(q\frac{3\pi}{4}M) + 2\cos(\frac{n\pi}{6})J_n(q\frac{\sqrt{3}\pi}{4}M)\} \\ & + \sum_{\substack{k=1 \\ k \neq -n}}^{\infty} \frac{1}{n+k} \cos(m\frac{\pi}{2}) \sin(k\frac{\pi}{2}) \cos\left([n+k]\frac{\pi}{2}\right) \sin\left([n+k]\frac{\pi}{6}\right) \\ & \times \left\{ J_k(q\frac{3\pi}{4}M) \sin\left([n+3k]\frac{\pi}{3}\right) - 2\cos(n\frac{\pi}{6}) \sin\left([n-3k]\frac{\pi}{6}\right) \left\{ J_k(q\frac{\sqrt{3}\pi}{4}M) \right\} \right. \\ & \left. + \sum_{\substack{k=1 \\ k \neq n}}^{\infty} \frac{1}{n-k} \cos(m\frac{\pi}{2}) \sin(k\frac{\pi}{2}) \cos\left([n-k]\frac{\pi}{2}\right) \sin\left([n-k]\frac{\pi}{6}\right) \right. \\ & \left. \times \left\{ J_k(q\frac{3\pi}{4}M) \sin\left([n-3k]\frac{\pi}{3}\right) - 2\cos(n\frac{\pi}{6}) \sin\left([n+3k]\frac{\pi}{6}\right) \left\{ J_k(q\frac{\sqrt{3}\pi}{4}M) \right\} \right\} \right) \end{aligned} \right) \tag{30}$$

where V_{dc} is the dc-link voltage, M is the modulation index, and $q = m + n(\omega_0/\omega_c)$.

and in AZSPWM. Therefore, the NWTHTD of SVM is the same as that of the AZSPWM. Similarly, the NWTHTD in the case of the NSPWM in the linear modulation range ($0.769 \leq M < 2/\sqrt{3}$) is the same as the DPWM1. Although NSPWM is a discontinuous PWM scheme, it demonstrates better harmonic performance compared to the AZSPWM. Therefore, the use of the NSPWM results in a improved harmonic performance and reduced switching losses. In order to operate the VSCs in the full modulation range, AZSPWM in the low modulation index range ($0 \leq M < 0.769$) and NSPWM in the high modulation index range ($0.769 \leq M < 2/\sqrt{3}$) can be used.

V. DESIGN OF INTEGRATED INDUCTOR

Design steps are illustrated by deriving design equations of an integrated inductor for an active three-phase rectifier.

A. Design Procedure

Design steps of an integrated inductor for an active three-phase rectifier are illustrated. The flux in the integrated inductor is highly influenced by the PWM scheme used. For the active rectifier applications, the modulation index varies

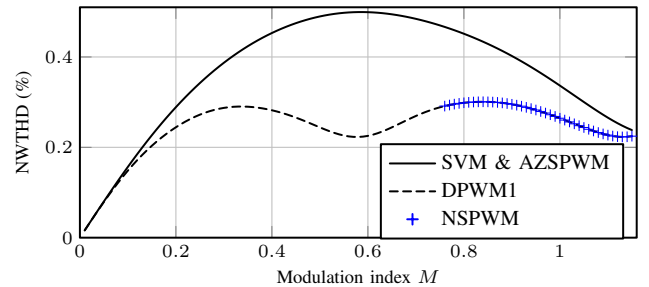


Fig. 11. Theoretical variation of the NWTHTD with a modulation index M of the parallel interleaved VSCs with an interleaving angle of 180° .

in close vicinity to one. Therefore, the use of the NSPWM is considered due to its superior harmonic performance and lower switching losses. The relevant design equations are derived hereafter.

1) *Value of the Line Filter Inductor:* The value of a line filter inductor L_f is generally chosen to limit the peak-to-peak value of the ripple component of the resultant line current to

an acceptable value. Let

$$k = \frac{\Delta I_{x,m}}{I_{x,p}} \quad (32)$$

where $\Delta I_{x,m}$ is the maximum value of the peak-to-peak ripple current component of the resultant line current and $I_{x,p}$ is the amplitude of the fundamental component of the resultant line current. For the NSPWM, the peak-to-peak value of the ripple current component is maximum for the modulation index of $M = 1$ and at the reference voltage space vector angle of $\psi = 0^\circ$ [19] (and $\psi = 180^\circ$) and it is given as

$$\Delta I_{x,m} = \frac{V_{dc}}{24f_c L_f} \quad (33)$$

Using (32) and (33), the value of the line filter inductor can be obtained as

$$L_f = \frac{V_{dc}}{24f_c k I_{x,p}} \quad (34)$$

2) *Maximum Flux Density in Bridge Legs:* The flux density in the bridge legs is obtained using (8), (17), and (34) and it is given as

$$B_{bl}(t) = \frac{V_{dc}(2+k)}{48Nf_c k A_{c,bl}} \cos(\psi + \gamma) \quad (35)$$

where $A_{c,bl}$ is the cross-section area of the bridge leg and γ is the power factor angle. For the active rectifier, γ is considered to be zero. Therefore, the flux density in the bridge leg is maximum at $\psi = 0^\circ$ and it is obtained as

$$B_{bl,m} = \frac{V_{dc}(2+k)}{48Nf_c k A_{c,bl}} \quad (36)$$

3) *Maximum Flux Density in Common Legs:* Obtaining the value of the $I_{CM,c}$ from (19) and substituting in (7) yields

$$B_{cl} = \frac{\lambda_{CM}}{2NA_{c,cl}} \quad (37)$$

where $A_{c,cl}$ is the cross-section area of the Common leg. Substituting the value of λ_{CM} from Table I into (37) yields

$$B_{cl} = \frac{V_{dc}}{32Nf_c A_{c,cl}} \left(3M \sin[\arccos(\frac{1}{\sqrt{3}M})] - 1 \right) \quad (38)$$

The flux density in the common leg is maximum for the modulation index $M = M_{max}$ and it is given as

$$B_{cl,m} = B_{cl} |_{M=M_{max}} \quad (39)$$

where M_{max} is the maximum value of the modulation index in the given operating range.

4) *Maximum Flux Density in Phase Legs:* Obtaining the values of the $I_{x,c}$ and $I_{CM,c}$ from (19) and substituting in (6) yields

$$\phi_{x1}(t) = \frac{1}{N} L_f I_x(t) + \frac{1}{2N} \int \Delta V_x dt \quad (40)$$

As evident from (40), the flux in the phase leg has two distinct component:

- 1) Resultant flux component ϕ_x .
- 2) Circulating flux component $\phi_{x,c}$.

The resultant flux component ϕ_x is equal to the flux through the bridge leg. ϕ_x attains its maximum value for reference

voltage space vector angle $\psi = 0^\circ$ and can be readily obtained from (36). The circulating flux component $\phi_{x,c}$ is proportional to the $\int \Delta V_x dt$. The peak value of the $\int \Delta V_x dt$ is different in each sampling interval due to the change in the dwell times of the corresponding voltage vectors. For the NSPWM, the circulating flux component attains maximum value at the reference voltage space vector angle ψ_m and it is given as

$$\phi_{x,c,max} = \phi_{x,c}(t) |_{\psi=\psi_m} = \frac{V_{dc}}{8Nf_c} \quad (41)$$

$$\psi_m = 120^\circ - \arcsin\left(\frac{1}{\sqrt{3}M_{min}}\right) \quad (42)$$

where M_{min} is the minimum value of the modulation index in the given operating range. Flux in the phase leg

$$\phi_{x1}(t) = \phi_x(t) + \phi_{x,c}(t) \quad (43)$$

and for the phase A , it could attain its maximum value at $\psi = 0^\circ$, $\psi = \psi_m$, or $\psi = 30^\circ$. The flux density in the phase leg at these values of the reference voltage space vector angle is given as

$$\begin{aligned} B_{A1}(t) |_{\psi=0^\circ} &= \frac{V_{dc}(2+k)}{48Nf_c k A_{c,pl}} \\ B_{A1}(t) |_{\psi=30^\circ} &= \frac{V_{dc}}{4Nf_c A_{c,pl}} \left(1 + \frac{\sqrt{3}}{2} \left[\frac{2+k}{12k} - M_{min} \right] \right) \\ B_{A1}(t) |_{\psi=\psi_m} &= \frac{V_{dc}}{8Nf_c A_{c,pl}} \left(1 + \frac{2+k}{6k} \cos \psi_m \right) \end{aligned} \quad (44)$$

where $A_{c,pl}$ is the cross-section area of the phase leg. The maximum value of the flux density in the phase leg is obtained from (44) and it is given as

$$B_{pl,m} = \max(B_{A1} |_{\psi=0^\circ}, B_{A1} |_{\psi=30^\circ}, B_{A1} |_{\psi=\psi_m}) \quad (45)$$

5) *Number of Turns and Cross-section Area of the Cores:* Once the material for the magnetic core is chosen, value of the $B_{pl,m}$ is selected such that $B_{pl,m} < B_{sat}$, where B_{sat} is the saturation flux density. The value of the $N \times A_{c,pl}$ can be obtained using (44) and (45) and the number of turns and the cross-section area of the core is selected using this value. Once the value of the number of turns N is known, the cross-section area of the bridge legs and the common legs can be obtained using (36) and (39), respectively. The air gap cross-section can be obtained from the dimensions of the phase leg and the bridge leg. Using the value of the air gap cross-section and (18), the length of the air gap can be obtained.

B. Comparative Evaluation

The size reduction is achieved by using the integrated inductor and it is demonstrated by comparing the volume of the integrated inductor with the volume of the magnetic component of a system, which uses two separate inductors, one for the circulating current suppression and another for reducing the ripple in the line current for each of the phases, as shown in Fig. 1.

1) *Coupled Inductor*: The maximum value of the product of the number of turns and the cross-section area of the core is given as

$$N_{CI}A_{c,CI} = \frac{V_{dc}}{8f_c B_{CI,m}} \quad (46)$$

where N_{CI} is the number of turns of each coil of the CI, $B_{CI,m}$ is the maximum permissible value of the flux density, and $A_{c,CI}$ is the cross-section area of the central leg of the CI. The cross-section area of the side legs is half than that of the central leg.

2) *Line Filter Inductor*: The maximum value of the product of the number of turns and the cross-section area is

$$N_{L_f}A_{c,L_f} = \frac{V_{dc}(2+k)}{48f_c k B_{L_f,m}} \quad (47)$$

where N_{L_f} is the number of turns in the line filter inductor, $B_{L_f,m}$ is the maximum flux density, and A_{c,L_f} is the cross-section area of the central leg of the line filter inductor.

3) *Comparison*: The number of turns N and the cross-section area of the phase leg $A_{c,pl}$ of the integrated inductor is taken as base values for the comparison.

For the specified modulation range (the modulation index is assumed to be $0.9(M_{min}) \leq M \leq 1.1(M_{max})$), $\psi_m = 80^\circ$ and $B_{pl,m} = B_{A1} |_{\psi=\psi_m}$. The maximum value of the $N \times A_{c,pl}$ is given as

$$NA_{c,pl} = \frac{V_{dc}}{8f_c B_{pl,m}} \left(1 + \frac{2+k}{35k}\right) \quad (48)$$

Assuming $A_{c,pl} = A_{c,CI}$ and taking $k = 0.35$, the relationship between N and N_{CI} is obtained using (46) and (48) as it is given by

$$N = 1.19N_{CI} \quad (49)$$

As coils in both the cases should be designed to carry the same current, it is evident from (49) that for the $A_{c,pl} = A_{c,CI}$, the volume of the winding material in the integrated inductor is 19% higher than that of the CI. However, the separate inductor based solution requires additional coils for the line filter inductor, which should be designed to carry the rated current.

Assuming $B_{L_f,m} = B_{pl,m}$ and using (47) and (48), the relationship between the parameters of the separate line filter inductor and the integrated inductor is derived as

$$\frac{N_{L_f}A_{c,L_f}}{NA_{c,pl}} = 0.94 \quad (50)$$

Taking $N_{L_f} = 0.67N$ gives

$$A_{c,L_f} = 1.4A_{c,pl} \quad (51)$$

For the given value of the M_{max} , the maximum value of the $N \times A_{c,cl}$ can be obtained using (38) and (39) and it is given as

$$NA_{c,cl} = \frac{1.8V_{dc}}{32f_c B_{cl,m}} \quad (52)$$

Assuming $B_{cl,m} = B_{pl,m}$ and using (48) and (52), the relationship between the cross-section area of the common leg and the cross-section area of the phase leg is obtained as

$$A_{c,cl} = 0.4A_{c,pl} \quad (53)$$

TABLE IV
PARAMETERS FOR THE SIMULATIONS AND THE EXPERIMENTAL STUDIES

Parameters	Values
Power	3 KVA
DC-link voltage V_{dc}	650 V
Switching frequency f_c	4.95 kHz
Line filter inductance L_f	2.4 mH
Circulating current inductance L_c	94 mH
Interleaving angle	180°

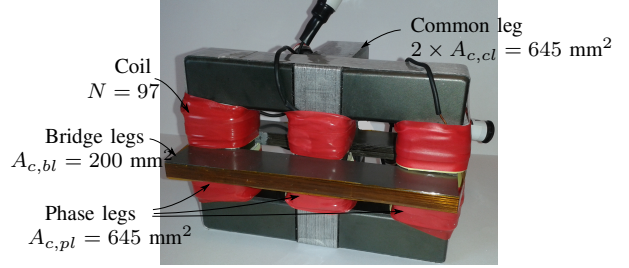


Fig. 12. Image of the implemented integrated inductor.

Therefore, the total cross-section area of both of the common legs is 80% of the cross-section area of a phase leg. Using (36) and (48), the relationship between the $A_{c,bl}$ and the $A_{c,pl}$ is obtained as

$$A_{c,bl} = 0.94A_{c,pl} \quad (54)$$

Using these derivations, the volume of the proposed integrated inductor is compared with the state-of-the-art filter arrangement. The maximum value of the flux density of the magnetic cores and the current density are taken to be the same in both the cases. In this scenario, the integrated inductor results in 39% saving in copper and 35% reduction in the magnetic material.

VI. SIMULATION AND EXPERIMENTAL RESULTS

A. Simulation Study

The system parameters that are used for the simulations and the experimental studies are listed in Table IV. The phase legs and the common legs of the integrated inductor are realized using three U shape (0R49925UC) and one I shape (0R49925IC) ferrite cores from Magnetics, as shown in Fig. 12. Instead of using two common legs with the cross-section area of $A_{c,cl}$, single common leg having the cross-section area of $2 \times A_{c,cl}$ is used. The bridge legs are realized using the laminated steel block. The implemented inductor and the inductor shown in Fig. 2(a) are magnetically equivalent and the use of the inductor shown in Fig. 12 does not impair the significance of the analysis and the obtained experimental results.

Time domain simulations have been carried out using PLECS. The flux density in the various parts of the integrated inductor in the case of the NSPWM, are shown in Fig. 13. The fundamental frequency component of the flux density in both the upper and the lower part of the phase legs is the same. Whereas, the circulating flux component has the same magnitude but opposite polarity, as shown in Fig. 13(a) and 13(b). The flux density in the air gap (which is the

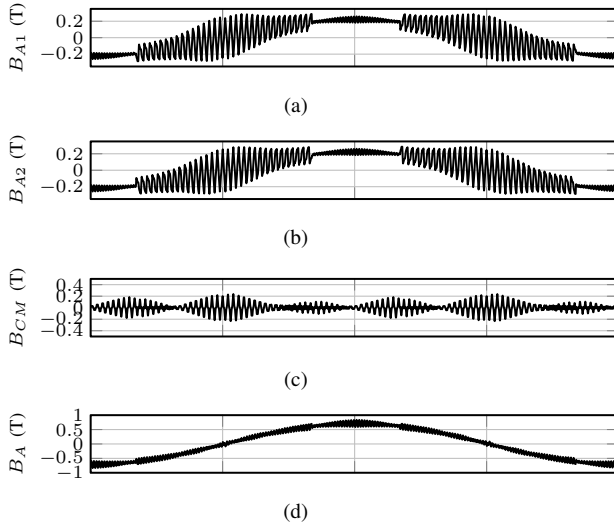


Fig. 13. NSPWM: Flux density waveforms for modulation index of $M = 1$. (a) Flux density in the upper part of the phase leg, (a) Flux density in the lower part of the phase leg, (c) Flux density in the common leg, (d) Air gap flux density.

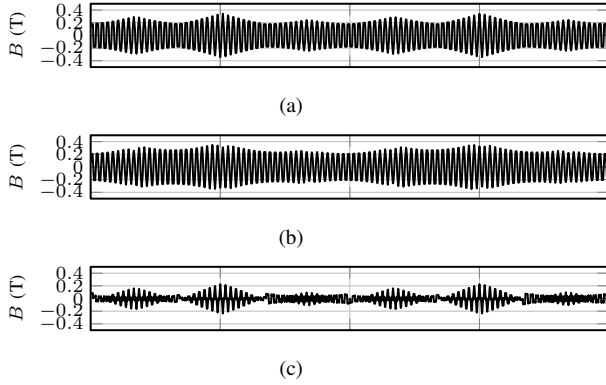


Fig. 14. Flux density in the common leg for $M = 1$. (a) SVM, (b) DPWM1, (c) AZSPWM.

same as the flux density in the bridge leg) has predominant fundamental frequency component, as shown in Fig. 13(d).

The flux density waveform in the common leg for the different PWM schemes is shown in Fig. 14 for the modulation index $M = 1$. The use of both the SVM and the DPWM1 results in the maximum value of the B_{CM} close to 0.35 T. On the other hand, the maximum value of the B_{CM} is 0.25 T in the case of the NSPWM. The use of the AZSPWM results in a maximum value of the B_{CM} to be 0.22 T.

B. Hardware Results

The PWM schemes are realized by the scalar implementation using TMS320F28346 floating-point digital signal processor. The output terminals are connected to a three-phase resistive load of 53Ω . The line current I_x , the circulating current $I_{x,c}$, and the CM circulating current $I_{CM,c}$ for the NSPWM and the AZSPWM are shown in Fig. 15(a), and 16(a), respectively. It is evident from these results that the integrated inductor offers the desired inductance to the line

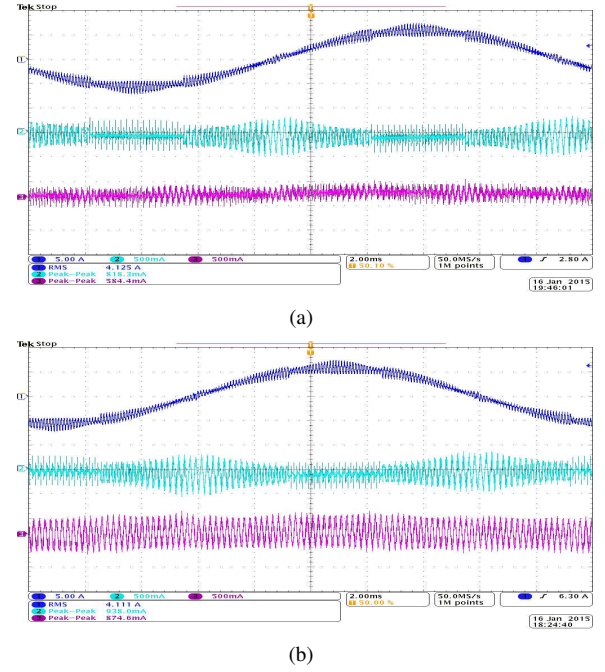


Fig. 15. Measured currents at modulation index of $M = 1$. Ch1: Phase A line current (5 A/div), Ch2: Phase A circulating current ($2 \times I_{A,c}$) (0.5 A/div), Ch3: CM circulating current ($I_{A1} + I_{B1} + I_{C1} = 3 \times I_{CM,c}$) (0.5 A/div). (a) NSPWM, (b) DPWM1.

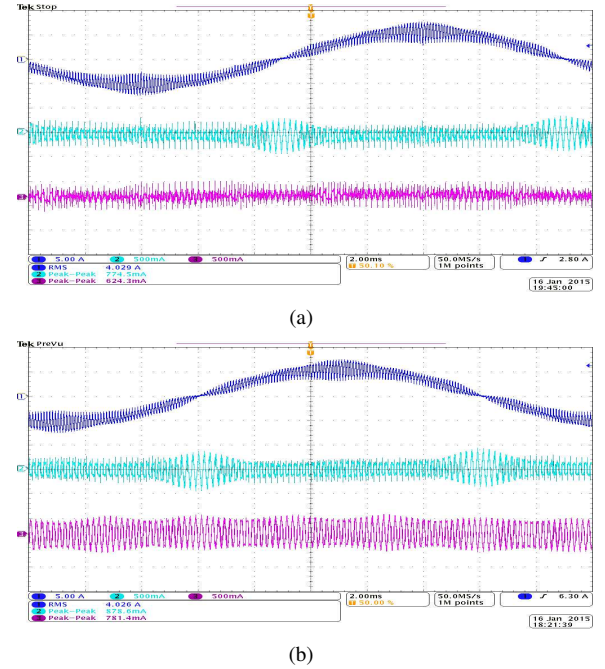


Fig. 16. Measured currents at modulation index of $M = 1$. Ch1: Phase A line current (5 A/div), Ch2: Phase A circulating current ($2 \times I_{A,c}$) (0.5 A/div), Ch3: CM circulating current ($I_{A1} + I_{B1} + I_{C1} = 3 \times I_{CM,c}$) (0.5 A/div). (a) AZSPWM, (b) SVM.

current and also suppresses the circulating current. The current waveforms for the DPWM1 is shown in Fig. 15(b). From Fig. 15, it is clear that the resultant line current I_x and the circulating current $I_{x,c}$ are similar in case of the NSPWM and the DPWM1. However, the CM circulating current $I_{CM,c}$ in

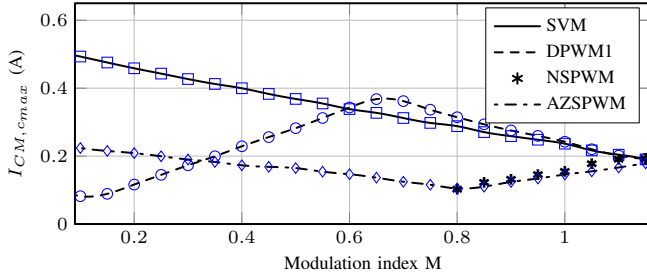


Fig. 17. Measured maximum values of the CM circulating current over a fundamental cycle as a function of the modulation index. For the NSPWM, the values are plotted only for the linear modulation range of $0.769 \leq M \leq 1.154$.

the case of the NSPWM is very small compared to that of the DPWM1. Similarly, the line current quality in the case of the AZSPWM and the SVM is the same, as it is evident from Fig. 16. However, the use of the AZSPWM would result in less CM circulating current compared to that of the SVM.

It has been analytically shown that the peak value of the CM flux can be reduced by using the NSPWM and the AZSPWM. This has been verified by measuring the sum of the currents of all the three phases of the first VSC. As defined in (4), the sum of the currents of all the three phases of the first VSC is equal to the $3I_{CM,1}$. Since $I_{CM,2} = -I_{CM,1}$, substituting this in (5) yields

$$I_{A1} + I_{B1} + I_{C1} = 3I_{CM,1} = 3I_{CM,c} \quad (55)$$

Using (22), (23), and (55) the sum of the currents of all the three phases of the first VSC is obtained as

$$I_{A1} + I_{B1} + I_{C1} = \frac{4\Re_L}{N^2} \lambda_{CM} \quad (56)$$

As the sum of the current of all the three phases of the first VSC is proportional to the CM flux, set of readings of this value were obtained with the dc-link voltage of 325 V and a resistive load of 27 Ω . The dc-link voltage value is reduced to half to obtain these sets of readings, as the use of the SVM at the low modulation indices with the rated dc-link voltage causes the saturation of the designed integrated inductor due to high CM flux (as analyzed in this paper and shown in Fig. 7). The variation of the maximum value of the CM circulating current with the modulation index is shown in Fig. 17, which is in a good agreement with the analysis presented in a section III.

It has been analytically shown in section IV that the AZSPWM is harmonically equivalent to the SVM. Similarly, it is also established that the harmonic performance of the NSPWM is same as that of the DPWM1. This has been demonstrated by evaluating the NWTHTD of the resultant line-to-line voltage ($V_{A'B'}$) using the analytical expressions of the harmonic coefficients A_{mn} and B_{mn} . However, A' and B' are the fictitious terminals and not available for measurement (refer Fig. 3). Therefore, the harmonic performance of the PWM scheme has been indirectly verified by measuring the total harmonic distortion of the resultant line current as a function of the modulation index is shown in

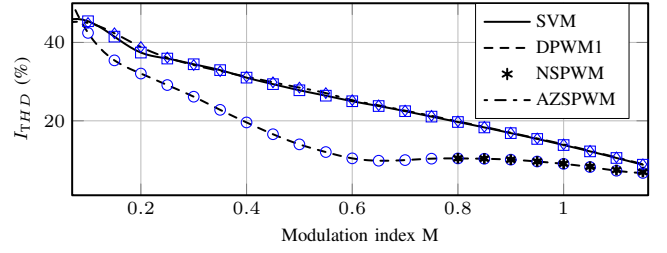


Fig. 18. Measured total harmonic distortion of the resultant line current as a function of the modulation index. For the NSPWM, the values are plotted only for the linear modulation range of $0.769 \leq M \leq 1.154$.

Fig. 18. For any given modulation index, the I_{THD} values for the AZSPWM closely matched with that of the SVM. Similarly, the harmonic performance of NSPWM in its linear modulation range is the same as that of the DPWM1. It is also clear from Fig. 18 that the NSPWM and the DPWM1 are harmonically superior than the AZSPWM and the SVM, which is in agreement with the NWTHTD results shown in Fig. 11.

VII. CONCLUSION

In this paper, the integrated inductor for the parallel interleaved VSCs is presented. The proposed inductor combines the functionality of both the line filter inductor and the circulating current filter inductor. A five leg magnetic structure is proposed, where the outer two legs provide low reluctance path for the CM flux. A PWM scheme, which employs AZSPWM in the low modulation index range ($0 \leq M < 0.769$) and NSPWM in the high modulation index range ($0.769 \leq M < 2/\sqrt{3}$) is analyzed for the parallel interleaved VSCs. It reduces the maximum value of the CM flux-linkage by 68 % compared to that of the SVM and 52 % compared to that of the DPWM1. The harmonic performance of the NSPWM and the AZSPWM for the parallel interleaved VSCs is also analyzed and it is established that the magnitude of the harmonic frequency components in the NSPWM is the same as that of the DPWM1 for an interleaving angle of 180° . Similarly, the harmonic performance of the AZSPWM is the same as that of the SVM. Therefore, the use of the NSPWM and the AZSPWM result in flux reduction in the common legs of the integrated inductor, without compromising the harmonic performance.

Procedure for designing the integrated inductor is also presented. The design equations are derived for the active three-phase rectifier application. The volume of the magnetic core and the copper of the proposed integrated inductor is compared with the converter system, having separate CI and the line filter inductor for each of the phases. When used with the NSPWM, the integrated leads to 35% reduction in magnetic core and 39% saving in copper.

REFERENCES

- [1] F. Ueda, K. Matsui, M. Asao, and K. Tsuboi, "Parallel-connections of pulsewidth modulated inverters using current sharing reactors," *IEEE Trans. Power Electron.*, vol. 10, no. 6, pp. 673–679, Nov 1995.
- [2] L. Asiminoaei, E. Aeloiza, P. N. Enjeti, and F. Blaabjerg, "Shunt active-power-filter topology based on parallel interleaved inverters," *IEEE Trans. Ind. Electron.*, vol. 55, no. 3, pp. 1175–1189, 2008.

- [3] D. Zhang, F. Wang, R. Burgos, L. Rixin, and D. Boroyevich, "Impact of interleaving on AC Passive Components of Paralleled Three-Phase Voltage-Source Converters," *IEEE Trans. Power Electron.*, vol. 46, no. 3, pp. 1042–1054, 2010.
- [4] H. Akagi, A. Nabae, and S. Atoh, "Control strategy of active power filters using multiple voltage-source PWM converters," *IEEE Trans. Ind. Appl.*, vol. 1A-22, no. 3, pp. 460–465, 1986.
- [5] I. G. Park and S. I. Kim, "Modeling and analysis of multi-interphase transformers for connecting power converters in parallel," in *Proc. of 28th Annual IEEE Power Electronics Specialists Conference, 1997. PESC '97*, vol. 2, Jun 1997, pp. 1164–1170 vol.2.
- [6] B. Cougo, T. Meynard, and G. Gateau, "Parallel three-phase inverters: Optimal PWM method for flux reduction in intercell transformers," *IEEE Trans. Power Electron.*, vol. 26, no. 8, pp. 2184–2191, Aug 2011.
- [7] J. Ewanchuk and J. Salmon, "Three-limb coupled inductor operation for paralleled multi-level three-phase voltage sourced inverters," *IEEE Trans. Ind. Electron.*, vol. 60, no. 5, pp. 1979–1988, 2013.
- [8] D. G. Holmes and T. A. Lipo, *Pulse Width Modulation for Power Converters: Principles and Practice*. Hoboken, NJ: Wiley-IEEE Press, 2003.
- [9] G. Gohil, R. Maheshwari, L. Bede, T. Kerekes, R. Teodorescu, M. Liserre, and F. Blaabjerg, "Modified discontinuous pwm for size reduction of the circulating current filter in parallel interleaved converters," *IEEE Trans. Power Electron.*, vol. 30, no. 7, pp. 3457–3470, July 2015.
- [10] C.-C. Hou, C.-C. Shih, P.-T. Cheng, and A. M. Hava, "Common-mode voltage reduction pulsewidth modulation techniques for three-phase grid-connected converters," *IEEE Trans. Power Electron.*, vol. 28, no. 4, pp. 1971–1979, April 2013.
- [11] G. Oriti, A. Julian, and T. Lipo, "A new space vector modulation strategy for common mode voltage reduction," in *Proc. of 28th Annual IEEE Power Electronics Specialists Conference*, vol. 2, Jun 1997, pp. 1541–1546 vol.2.
- [12] Y.-S. Lai and F.-S. Shyu, "Optimal common-mode voltage reduction PWM technique for inverter control with consideration of the dead-time effects-part I: basic development," *IEEE Trans. Ind. Appl.*, vol. 40, no. 6, pp. 1605–1612, 2004.
- [13] Y.-S. Lai, P.-S. Chen, H.-K. Lee, and J. Chou, "Optimal common-mode voltage reduction PWM technique for inverter control with consideration of the dead-time effects-part ii: applications to im drives with diode front end," *IEEE Trans. on Ind. Appl.*, vol. 40, no. 6, pp. 1613–1620, 2004.
- [14] W. Hofmann and J. Zitzelsberger, "PWM-control methods for common mode voltage minimization - a survey," in *Proc. International Symposium on Power Electronics, Electrical Drives, Automation and Motion, 2006. SPEEDAM 2006.*, 2006, pp. 1162–1167.
- [15] M. Cacciato, A. Consoli, G. Scarcella, and A. Testa, "Reduction of common-mode currents in PWM inverter motor drives," *IEEE Trans. Ind. Appl.*, vol. 35, no. 2, pp. 469–476, 1999.
- [16] A. Hava and E. Un, "A high-performance PWM algorithm for common-mode voltage reduction in three-phase voltage source inverters," *IEEE Trans. Power Electron.*, vol. 26, no. 7, pp. 1998–2008, 2011.
- [17] E. Un and A. Hava, "A near-state PWM method with reduced switching losses and reduced common-mode voltage for three-phase voltage source inverters," *IEEE Trans. Ind. Appl.*, vol. 45, no. 2, pp. 782–793, 2009.
- [18] A. Hava and N. Cetin, "A generalized scalar pwm approach with easy implementation features for three-phase, three-wire voltage-source inverters," *IEEE Trans. Power Electron.*, vol. 26, no. 5, pp. 1385–1395, May 2011.
- [19] G. Gohil, L. Bede, R. Teodorescu, T. Kerekes, and F. Blaabjerg, "Line filter design of parallel interleaved VSCs for high power wind energy conversion system," *IEEE Trans. Power Electron.*, [Online early access], DOI: 10.1109/TPEL.2015.2394460, 2015.



Ghanshyamsinh Gohil (S'13) received the M.Tech. degree in electrical engineering with specialization in power electronics and power systems from the Indian Institute of Technology-Bombay, Mumbai, India, in 2011.

He is currently working towards the Ph.D. degree at the Department of Energy Technology, Aalborg University, Denmark. His research interests include parallel operation of voltage source converters, pulsewidth modulation techniques and the design of the inductive power components.



Lorand Bede (S'11) was born in Romania in 1989. He received the engineering degree in electrical engineering from Sapientia Hungarian University of Transilvania, Trgu Mure, Romania, 2011, the MSc. degree in Power Electronics and Drives from Aalborg University, Aalborg, Denmark, in 2013. Currently he is a PhD Fellow at the Department of Energy Technology, at Aalborg University, Aalborg. His research interest include grid connected applications based on parallel interleaved converters for wind turbine applications.



Remus Teodorescu (S'94-A'97-M'99-SM'02-F'12) received the Dipl.Ing. degree in electrical engineering from Polytechnical University of Bucharest, Romania in 1989, and PhD. degree in power electronics from University of Galati, Romania, in 1994. In 1998, he joined Aalborg University, Department of Energy Technology, power electronics section where he currently works as full professor. Since 2013 he is a visiting professor at Chalmers University. He has coauthored the book *Grid Converters for Photovoltaic and Wind Power Systems*, ISBN: 978-0-470-05751-3, Wiley 2011 and over 200 IEEE journals and conference papers. His areas of interests include: design and control of grid-connected converters for photovoltaic and wind power systems, HVDC/FACTS based on MMC, SiC-based converters, storage systems for utility based on Li-Ion battery technology. He was the coordinator of the Vestas Power Program 2008 2013.



Tamas Kerekes (S'06-M'09) obtained his Electrical Engineer diploma in 2002 from Technical University of Cluj, Romania, with specialization in Electric Drives and Robots. In 2005, he graduated the Master of Science program at Aalborg University, Institute of Energy Technology in the field of Power Electronics and Drives. In Sep. 2009 he obtained the PhD degree from the Institute of Energy Technology, Aalborg University. The topic of the PhD program was: "Analysis and modeling of transformerless PV inverter systems". He is currently employed as an

Associate professor and is doing research at the same institute within the field of grid connected renewable applications. His research interest include grid connected applications based on DC-DC, DC-AC single- and three-phase converter topologies focusing also on switching and conduction loss modeling and minimization in case of Si and new wide-bandgap devices.



Frede Blaabjerg (S'86-M'88-SM'97-F'03) was with ABB-Scandia, Randers, Denmark, from 1987 to 1988. From 1988 to 1992, he was a Ph.D. Student with Aalborg University, Aalborg, Denmark. He became an Assistant Professor in 1992, an Associate Professor in 1996, and a Full Professor of power electronics and drives in 1998. His current research interests include power electronics and its applications such as in wind turbines, PV systems, reliability, harmonics and adjustable speed drives.

He has received 15 IEEE Prize Paper Awards, the IEEE PELS Distinguished Service Award in 2009, the EPE-PEMC Council Award in 2010, the IEEE William E. Newell Power Electronics Award 2014 and the Villum Kann Rasmussen Research Award 2014. He was an Editor-in-Chief of the IEEE TRANSACTIONS ON POWER ELECTRONICS from 2006 to 2012. He has been Distinguished Lecturer for the IEEE Power Electronics Society from 2005 to 2007 and for the IEEE Industry Applications Society from 2010 to 2011. He is nominated in 2014 by Thomson Reuters to be between the most 250 cited researchers in Engineering in the world.